

Neutron-enhanced ion transport in cathode coating of Li-ion batteries

Ha M. Nguyen^{1,2,*,**}, Carson D. Ziemke^{1,3,**}, David Stalla⁵, Bikash Saha²,
Narendrakumar Narayanan², Sebastián Amaya-Roncancio⁵, Carlos
Wexler^{1,3}, John Gahl², Yangchuan Xing^{1,4,*}, and Thomas W. Heitmann^{1,2,3,*}

¹Materials Sciences and Engineering Institute, University of Missouri, Columbia, MO 65201,
USA

²University of Missouri Research Reactor (MURR), University of Missouri, Columbia, MO
65203, USA

³Department of Physics and Astronomy, University of Missouri, Columbia, MO 65201, USA

⁴Department of Chemical and Biomedical Engineering, University of Missouri, Columbia, MO
65201, USA

⁵Grupo de Simulación de Materiales, Escuela de Física, Universidad Pedagógica y Tecnológica
de Colombia, Avenida Central del Norte 39-115, Boyacá, 150003, Tunja, Colombia.

*Corresponding authors: hn4gq@missouri.edu, xingy@missouri.edu,
heitmannt@missouri.edu

**Authors with equal contributions

16th March 2026

Abstract

Polycrystalline solid-state ionic conductors (PolySSICs) are essential energy materials for all-solid-state Li-ion batteries (LIBs). To date, achieving a room-temperature ionic conductivity of solid electrolytes comparable to that ($\sigma \sim 10^{-2} - 10 \text{ S} \cdot \text{cm}^{-1}$) of their liquid successors remains a critical challenge. To address this, increasing research interest has recently been drawn in exploring a range of strategies to engineer

ion transport in PolySSICs. However, these methods indeed possess some strengths and limitations. Here, we experimentally demonstrate that thermal neutron irradiation can offer an innovative strategy in that neutron-induced modification in a model PolySSIC, LiBO_2 as an effective electrode coating of LIBs, can facilitate ion transport in the material, enhancing its ionic conductivity. The central concept is that high-flux ($\sim 10^9 \text{ neutrons} \cdot \text{cm}^{-2} \cdot \text{s}^{-1}$) thermal neutrons ($\sim 25 \text{ meV}$), harnessed at the Beam Port E (rather than the reactor core) of the University of Missouri Research Reactor (MURR), selectively transmute strong neutron absorbers ^{10}B and ^6Li isotopes, present at their natural abundances of $\sim 19.9\%$ and $\sim 7.5\%$, respectively, in polycrystalline grains of LiBO_2 , to generate lattice vacancies without compromising their crystallographic long-range order. In addition, by-product gamma photons emitted from ^{10}B transmutation free electrons to stop atomic displacement and simultaneously neutralize the space charge built up by positively-charged oxygen vacancies at grain boundaries. As a result, the ionic conductivity is increased by nearly 20% for the grains and more than 80% for the grain boundaries. This study validates theoretical predictions and highlights a vital strategy for controllably and selectively boosting ion transport channels in a variety of PolySSICs for solid ionic devices, including LIBs.

Keywords: Thermal neutron irradiation, nuclear engineering of defects in solids, lithium-ion batteries, solid electrolyte, cathode surface coating, solid-state ionic conductors, x-ray diffraction, scanning electron microscopy, electrochemical impedance spectroscopy, ionic conductivity, ion transport.

1. Introduction

The term solid state ionics was first introduced by Takehiko Takahashi in 1967 to describe the study of solid state ionic conductors (SSICs) and their technological applications [1–4]. These include inorganic polycrystalline SSICs (PolySSICs) that are capable of conducting electricity by transporting mobile charge carriers, involving ions, through grains and grain boundaries [3,5]. If the charge carriers are pure ions, PolySSICs are classified as fully ionic conductors. Examples of these conductors are solid electrolytes (SEs) [6]. In contrast, if PolySSICs are comprised of ions and electronic carriers (*e.g.*, electrons and electronic

holes), they are mixed ionic-electronic conductors (MIECs) [7–9] such as battery electrodes [10–15] and their coatings [16–31]. Regardless of whether a PolySSIC functions as a SE or a MIEC, fast ion transport is central to its effective performance in solid-state ionic devices [4, 32], including sensors [33, 34], detectors [35–37], actuators [38], ionic-migration-based resistive switching devices (resistive random access memories and memristors) [39, 40], electrochemical capacitors (supercapacitors) [41], fuel cells [42], and batteries [43, 44]. In this work, we focus on engineering ion transport in functional PolySSICs for their effective application in Li-ion batteries (LIBs), with the goal of enhancing their ionic conductivity.

Basically, one can find in any textbook on diffusion in crystalline solids [45–48] that, the ionic conductivity σ can be derived from the diffusivity D via the Nernst–Einstein relation, such that

$$\sigma = \frac{nq^2D}{k_{\text{B}}T}, \quad (1)$$

where n is the concentration of mobile charge carriers, q is the ionic charge, k_{B} is the Boltzmann constant, and T is the absolute temperature. Accordingly, σ is exponentially dependent on both the entropy of thermal activation ΔS and the enthalpy of thermal activation ΔH (also referred to as the activation energy E_{a} or migration energy barrier E_{m}) of diffusional processes [49, 50], following

$$\sigma \propto \exp\left(\frac{\Delta S}{k_{\text{B}}}\right) \exp\left(-\frac{\Delta H}{k_{\text{B}}T}\right). \quad (2)$$

In principle, Eq. (2) shows that σ can be exponentially enhanced by increasing ΔS while keeping ΔH constant, decreasing ΔH while keeping ΔS constant, or simultaneously increasing ΔS and decreasing ΔH . Nevertheless, despite the extensive body of work devoted to chemical and structural defect engineering in PolySSICs, most established approaches rely on equilibrium or near-equilibrium synthesis routes such as solid-state reaction methods in which defect populations are constrained by thermodynamic formation energies [51–67]. For example, Li-ion transport can be enhanced through several strategies, including the paddle-wheel mechanism, in which rotational motion of local anions [61] or electron pairs [62] facilitates diffusional jumps of Li^+ cations and thereby increases their diffusivity; introducing multiple cations and/or anions (e.g., a Li^+ -stuffing

strategy to enhance Li^+ – Li^+ repulsion) [63]; incorporating additional components into the host PolySSIC in a cocktail-like fashion [64, 65]; and introducing chemical, structural, or dynamical frustration—i.e., a physical condition in which numerous competing states exist with comparable energies [66, 67]. Collectively, these approaches aim to increase the configurational entropy of host PolySSICs, thereby promoting high-entropy PolySSICs with enhanced ion transport [55–59].

However, it is stressed that Deck and Hu stated in their recent review [60] that entropy-driven disorder improves Li^+ ion transport mainly by weakening local Li^+ –anion interactions, but high macroscopic ionic conductivity emerges only when this local disorder is integrated into thermodynamically stable long-range structures that enable percolating diffusion pathways. As a result, introducing a sufficiently high concentration of transport-enhancing lattice defects—particularly in chemically and structurally robust oxides—remains intrinsically challenging [68]. This limitation is especially pronounced for defect species with large formation energies, such as boron vacancies in LiBO_2 (the formation energy of boron vacancies is approximately 10 eV [23]), which have been theoretically predicted to substantially lower Li-ion migration barriers [$E_m = 0.27$ eV for the monoclinic LiBO_2 polymorph (*i.e.*, the α phase) and $E_m = 0.13$ eV for the tetragonal LiBO_2 polymorph (*i.e.*, the γ phase)] [23], yet are inaccessible through conventional chemical substitution or thermal processing routes.

An alternative way to overcome these thermodynamic constraints is to employ non-equilibrium methods capable of selectively generating lattice disorder while preserving long-range crystallographic order [23, 24, 68]. Particle irradiation represents one such approach, as it enables the dose-controlled introduction of point defects, defect clusters, and electronic excitations [69–78]. In particular, thermal neutron irradiation offers a unique and largely unexplored opportunity for defect engineering in PolySSICs, owing to its ability to induce selective nuclear transmutation reactions in specific isotopes naturally present or isotopically enriched in a concentration-controlled manner within the crystal lattice [79–87].

Here, we demonstrate for the first time that thermal neutron irradiation can serve as an effective and selective strategy to enhance ion transport in LiBO_2 , a model material

for PolySSICs that has been shown to function effectively as a cathode coating for both liquid- and solid-electrolyte LIBs [23–31] (see Refs. [23, 24] and references therein for a detailed review of recent studies on this material). Briefly, experimental reports have shown enhanced electrochemical performance and capacity retention in LiBO_2 -coated $\text{LiNi}_{0.8}\text{Mn}_{0.1}\text{Co}_{0.1}\text{O}_2$ cathodes, namely, 90.1% after 100 cycles at 1 C (3.0–4.6 V) [26], 82.1% after 100 cycles at 1 C and 4.5 V [27], and 84.3% after 150 cycles at 0.5 C [30]. Furthermore, doping boron into the cathode and coating it with LiBO_2 further enhances the performance, as shown by Gao *et al.* [28], who demonstrated significant improvements in cycling stability and capacity retention under various conditions.

In LiBO_2 , the presence of strong neutron absorbers ^6Li and ^{10}B provides a natural platform for neutron-induced engineering of ion transport in crystalline solids [69, 87]. The working principle for this approach is provided in Figure 1. The central concept is that high-flux thermal neutrons, harnessed at Beam Port E—rather than within the reactor core—of the University of Missouri Research Reactor (MURR), selectively induce nuclear transmutation of strong neutron absorbers, namely ^{10}B and ^6Li , which uniformly occupy the crystal lattice sites of LiBO_2 at their natural isotopic abundances of $\sim 19.9\%$ and $\sim 7.5\%$, respectively. These transmutation reactions (see Fig. 1) generate lattice vacancies while preserving long-range crystallographic order. In addition, gamma photons produced as by-products of ^{10}B transmutation [69, 70, 87, 88] liberate bonded electrons that mitigate atomic displacement through electron stopping mechanisms and simultaneously neutralize space-charge regions arising from positively charged oxygen vacancies at grain boundaries [36]. Consequently, ionic conductivity increases by nearly 20% within grains and by more than 80% across grain boundaries.

Beyond LiBO_2 , the approach presented here could establish a general framework for nuclear engineering of defects in PolySSICs, enabling access to defect configurations that are thermodynamically inaccessible via conventional synthesis routes. This strategy opens new avenues for simultaneously tuning enthalpic and entropic contributions to ion transport and provides a powerful complement to existing chemical and structural engineering methodologies for advanced solid-state ionic devices, including LIBs.

The organization of the main text of this work is as follows. After this brief Intro-

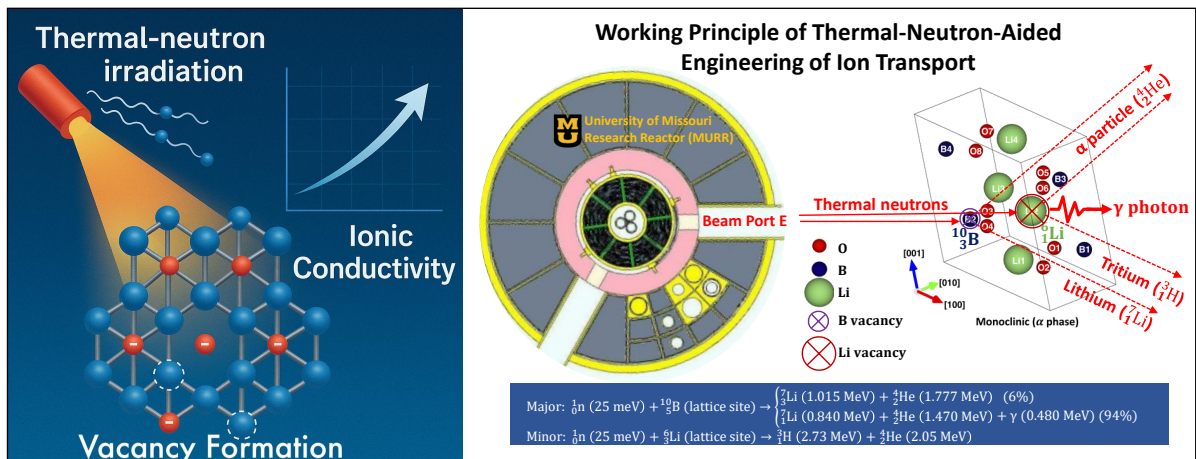


Figure 1: Working principle of thermal-neutron-irradiation approach to engineering of ion transport in LiBO_2 .

duction (Section 1), the main text then continues with Section 2 (Experimental Methods and Materials), which briefly describes the design of our proof-of-concept experiments, followed by Section 3 (Results and Discussions). Finally, the Conclusions (Section 4) summarizes the main findings and offers perspectives for future work.

2. Experimental Methods and Materials

Polycrystalline LiBO_2 pellets (coin-shaped, 1.6 cm in diameter and 0.3 cm in thickness) were synthesized from equal amounts of 0.5 grams of commercial anhydrous monoclinic LiBO_2 powder (Thermo, CAS No. 13453-69-5, Cat. No. 12591) by hot pressing (at 200°C under a load of 2.5 tons) followed by sintering in air for 48 hours at 663°C (75% of the melting point of monoclinic LiBO_2 phase). This heat treatment was carried out to fuse LiBO_2 fine grains together into dense polycrystalline solid pellets without full melting them while relieving internal stresses and improving the crystallinity of sintered gains. Afterward, the post-sintered pellets were stored in an inert gas glove box filled with either argon or helium gas.

Figure 2 shows the powder x-ray diffraction (PXRD) pattern (characterized on a Rigaku Ultima IV x-ray diffractometer) of the raw LiBO_2 powder, labeled as **raw (PXRD)**. Rietveld refinement indicates that the major phase (97%) is monoclinic LiBO_2 (space group $P2_1/c$), with lattice parameters $a = 5.83 \text{ \AA}$, $b = 4.34 \text{ \AA}$, $c = 6.44 \text{ \AA}$, $\beta = \gamma = 90^\circ$, and $\alpha = 114.96^\circ$. A minor secondary phase (3%) corresponding to tetragonal $\text{Li}_2\text{B}_4\text{O}_7$

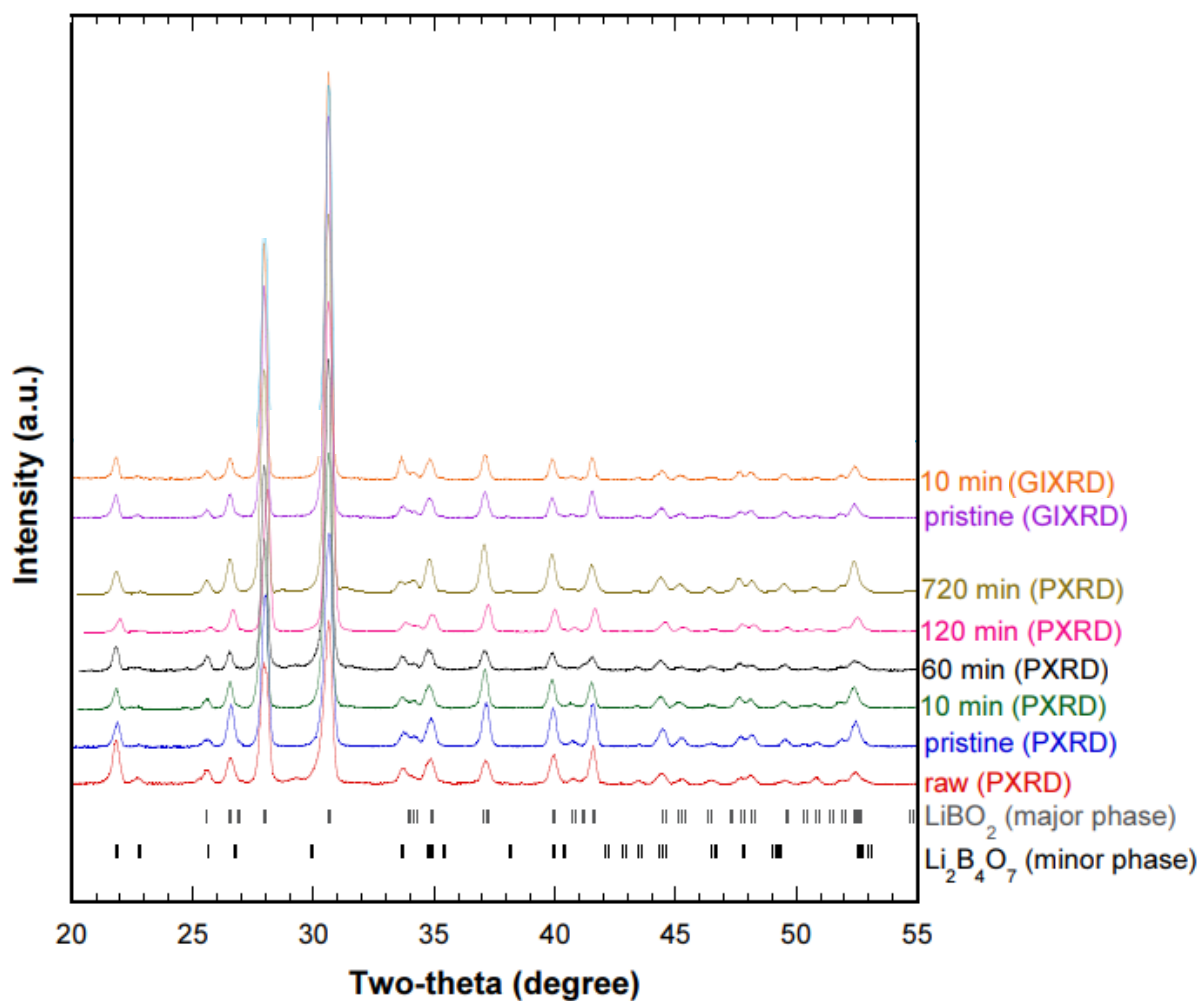
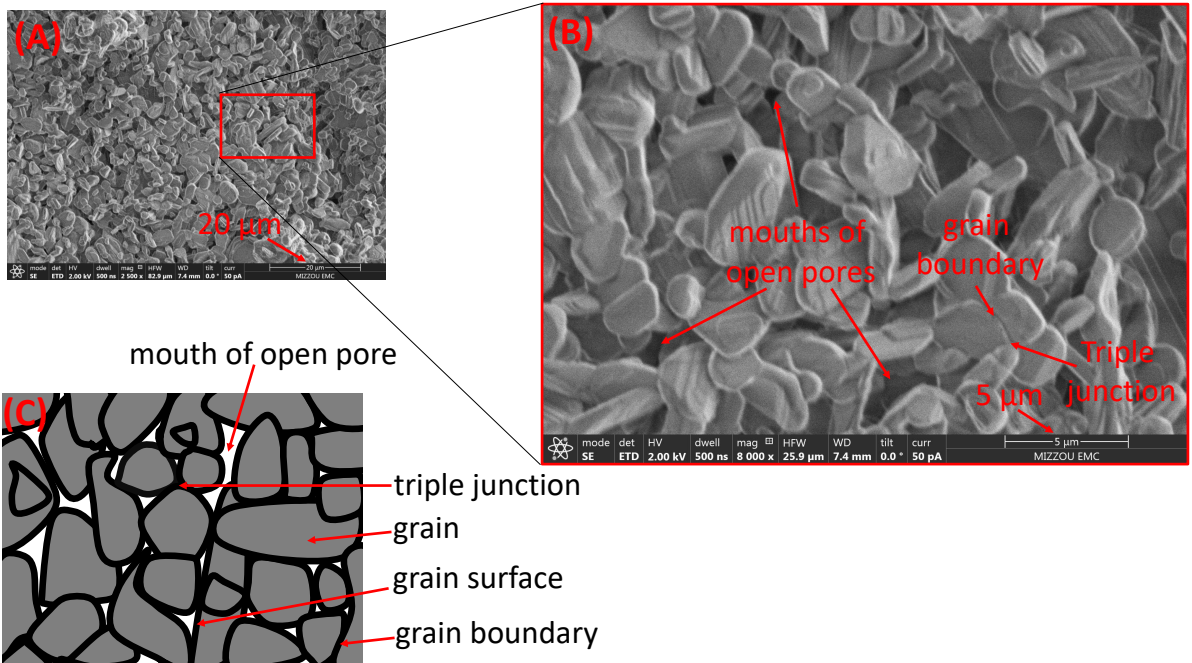


Figure 2: Powder x-ray diffraction (PXRD) and grazing incidence x-ray diffraction (GIXRD) patterns of raw, pristine, and irradiated samples of LiBO₂.

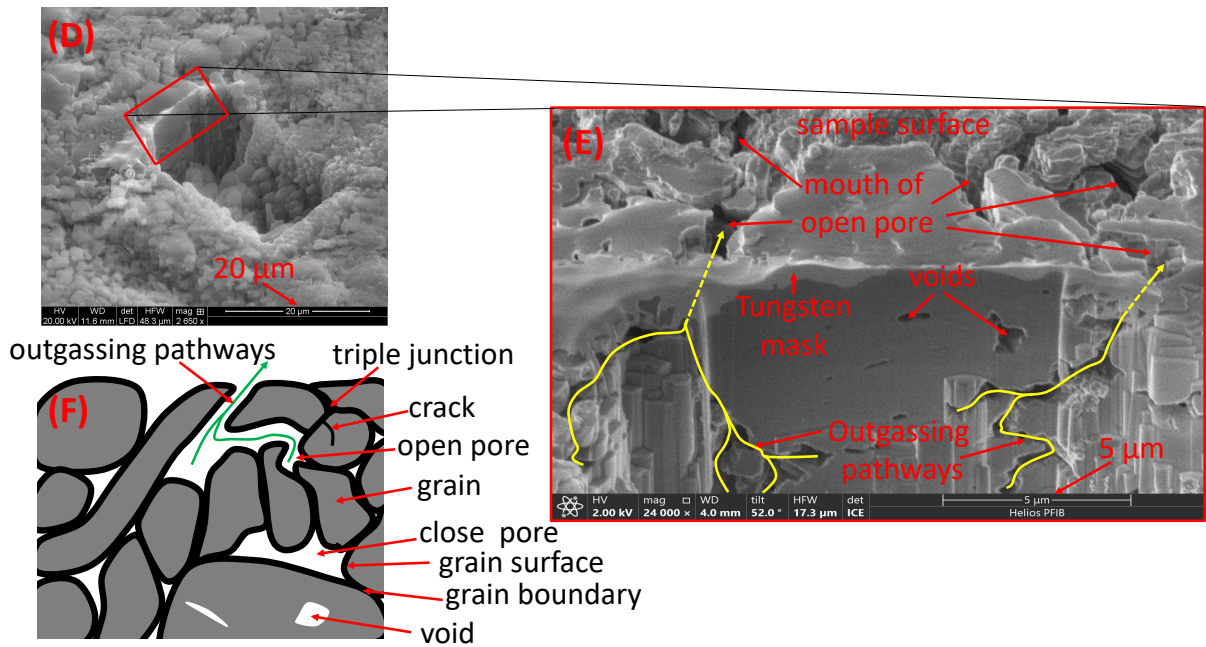
(space group $I4_1cd$) is also detected, with lattice parameters $a = b = 9.43 \text{ \AA}$ and $c = 10.28 \text{ \AA}$.

The PXRD pattern of powders obtained by grinding pristine pellets after sintering is also shown in Figure 2, labeled as **pristine (PXRD)**. Rietveld refinement again reveals monoclinic LiBO_2 as the dominant phase, with lattice parameters $a = 5.86 \text{ \AA}$, $b = 4.37 \text{ \AA}$, $c = 6.48 \text{ \AA}$, $\beta = \gamma = 90^\circ$, and $\alpha = 115.04^\circ$, along with a minor tetragonal $\text{Li}_2\text{B}_4\text{O}_7$ phase ($a = b = 9.44 \text{ \AA}$, $c = 10.45 \text{ \AA}$). At this stage, no additional crystalline phases are detected within the resolution of the Rietveld refinement. These results confirm that the sintering process preserves the monoclinic LiBO_2 phase of interest for subsequent characterization and neutron irradiation.

Thermal neutron irradiation was carried out at Beam Port E of MURR using a collimated thermal neutron beam (5-100 meV) with a flux of $\sim 10^9 \text{ neutrons}\cdot\text{cm}^{-2}\cdot\text{s}^{-1}$ [89–91]. Irradiations were performed outside the reactor core under controlled dose conditions, enabling increased throughput suitable for industrial-scale materials processing [92]. Pristine and irradiated pellets were characterized using PXRD on the aforementioned Rigaku Ultima IV x-ray diffractometer, grazing incidence x-ray diffraction (GIXRD) on a Philips X-Pert diffractometer, scanning electron microscopy (SEM) on a Thermo Scientific™ Scios™ 2 DualBeam™ Sy Focused Ion Beam Scanning Electron microscope, focused ion beam scanning electron microscopy (FIB-SEM) on a Thermo Scientific™ Helios™ 5 Hydra UX DualBeam microscope, and electrochemical impedance spectroscopy (EIS) measured using a Reference 3000 and Gamry’s EIS300 software and analyzed using Gamry’s Echem Analyst software. Comparative analysis of these data was used to evaluate irradiation-induced changes of the crystal structure, microstructure, and ion transport of LiBO_2 .



(a) SEM images



(b) FIB-SEM images

Figure 3: Microstructure of pristine LiBO_2 .

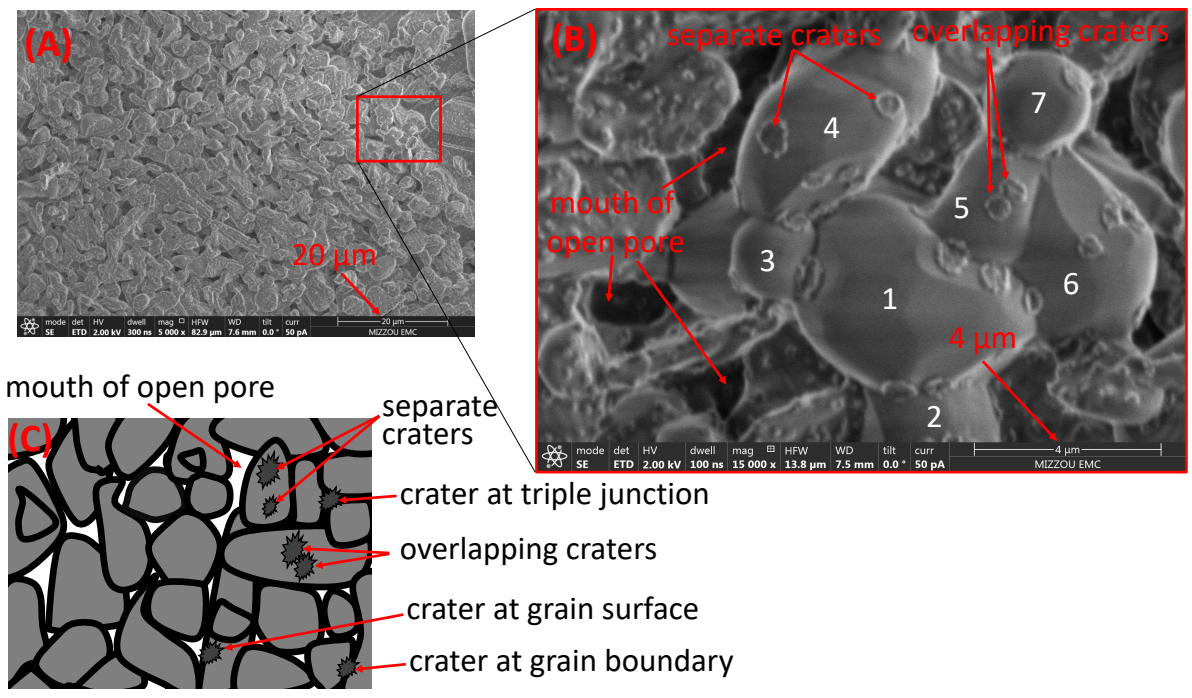
3. Results and Discussions

3.1 Structural and Microstructural Comparison: Pristine versus Low-Dose Irradiation

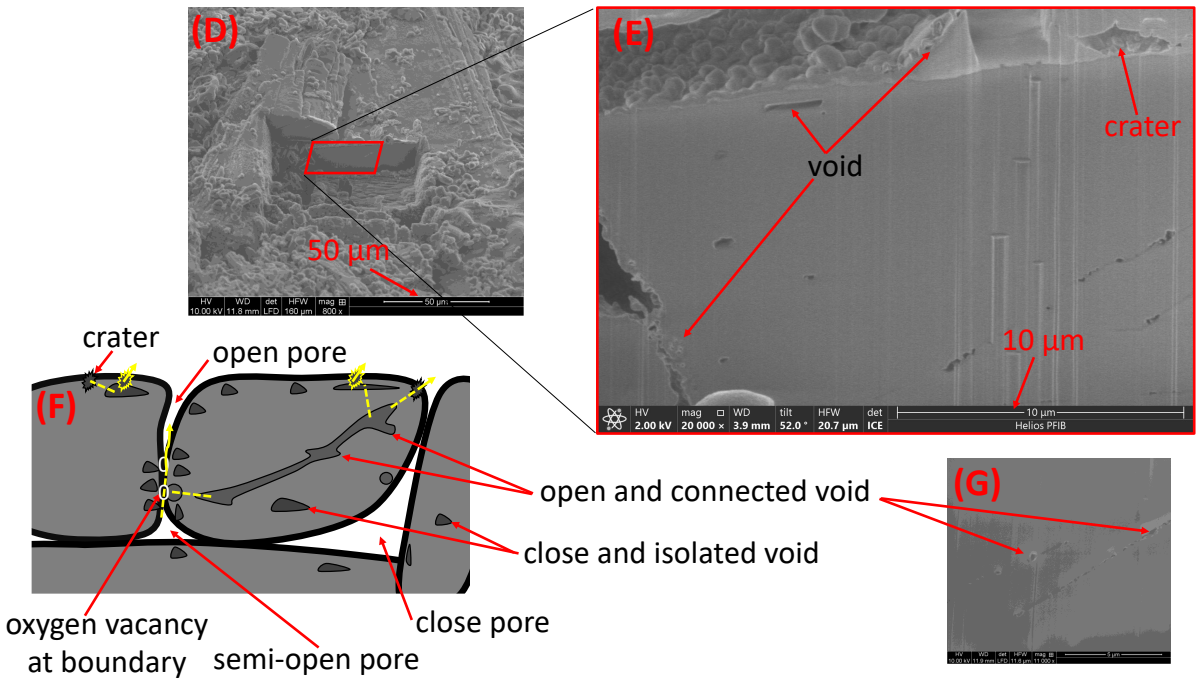
Figure 3 presents the microstructural features of pristine polycrystalline LiBO_2 pellets revealed by SEM and FIB-SEM analyses. Low-magnification SEM imaging (panel 3A) shows a dense polycrystalline microstructure composed of irregularly-shaped gravel-like grains with characteristic sizes on the order of several micrometers. Higher-magnification SEM images (panel 3B) resolve well-defined grain boundaries and frequent triple junctions, together with the mouths of open pores located predominantly at grain-boundary intersections. These features are schematically illustrated in Fig. 3C to clarify the geometric relationships among grains, grain boundaries, triple junctions, and open pores.

Cross-sectional FIB-SEM images (panels 3D,E) further reveal the subsurface microstructure, highlighting interconnected voids and open pores extending from the surface into the interior of the pellet. Notably, continuous pathways associated with grain boundaries, triple junctions, and microcracks are observed, forming potential outgassing or transport channels through the polycrystalline network. The schematic in panel 3F summarizes these features, distinguishing between open and closed pores, voids, and grain-boundary regions. Importantly, no evidence of abnormal grain growth, large cracks, or amorphous regions is observed in the pristine sample, indicating that the sintering process produces a mechanically intact and well-connected polycrystalline framework.

Overall, pristine LiBO_2 exhibits a dense polycrystalline microstructure comprising well-connected grains with clearly defined grain boundaries, triple junctions, and a limited amount of residual porosity. These microstructural features are expected to play a critical role by providing structurally well-defined transport pathways that can be selectively altered by subsequent neutron irradiation, as discussed below. Consequently, a detailed understanding of the pristine LiBO_2 's structure and microstructure is essential for interpreting the irradiation-induced modifications and the associated transport phenomena examined in this work.



(a) SEM images



(b) FIB-SEM images

Figure 4: Microstructure of 10-min-irradiated LiBO₂.

Figure 4 presents the microstructural evolution of LiBO_2 pellets after 10 min of thermal neutron irradiation, as revealed by SEM and FIB–SEM analyses. Low-magnification SEM imaging (panel 4A) shows that the overall polycrystalline framework remains intact, with no evidence of macroscopic cracking or amorphization. At higher magnification (panel 4B), however, numerous crater-like surface features are observed across grain surfaces, grain boundaries, and triple junctions.

The numbered grains (1–7) in panel 4B reveal pronounced grain-to-grain variability in both crater density and morphology. Certain grains (e.g., grain 5 and 6) exhibit multiple overlapping craters, whereas adjacent grains (e.g., grains 1 and 4) show comparatively fewer or more isolated features. This spatial heterogeneity indicates that crater formation is not uniformly distributed but is instead governed by local microstructural factors, such as crystallographic orientation, grain-boundary character, and proximity to pre-existing craters. In several cases, craters on neighboring grains appear spatially correlated across grain boundaries, suggesting cooperative microstructural evolution at triple junctions and interconnected pore networks rather than independent, isolated events.

These crater-like features occur both as isolated depressions and as overlapping structures and are frequently associated with the mouths of pre-existing open pores, indicating that neutron irradiation preferentially amplifies existing surface and subsurface defects. The schematic in panel 4C summarizes the spatial distribution of these irradiation-induced craters, emphasizing their preferential formation at microstructural heterogeneities such as grain boundaries, triple junctions, and open-pore interfaces.

The formation of these craters can be attributed to localized energy deposition following thermal neutron capture by ^6Li and ^{10}B . The resulting nuclear reactions generate energetic charged particles (e.g., α particles and recoil ions) with short penetration depths, leading to highly localized atomic displacement cascades, transient thermal spikes, and pressure buildup. When such events occur near free surfaces or mechanically weaker regions—such as pore mouths, grain boundaries, and triple junctions—the rapid release of energy can result in localized material ejection, producing crater-like depressions. The observed clustering and overlap of craters therefore reflect the coupling between neutron-induced energy deposition and pre-existing microstructural defects.

Cross-sectional FIB–SEM images (panels 4D,E) provide further insight into the sub-surface response to irradiation. Beneath surface craters, extended voids, partially open pores, and interconnected porosity are observed, indicating that neutron irradiation promotes the growth and interconnection of pre-existing voids rather than inducing uniform bulk damage. Continuous void pathways extending from the surface into the interior are evident in some regions, while other voids remain isolated, as schematically illustrated in panel 4F. These features suggest irradiation-enhanced mass transport and defect accumulation along grain boundaries and triple junctions. Importantly, grain interiors remain largely dense and structurally coherent, with no widespread cracking or grain fragmentation observed (panel 4G).

Overall, the 10-min thermal neutron irradiation induces highly localized microstructural modifications—manifested as surface craters, enlarged pore mouths, and connected void networks—while preserving the long-range integrity of the polycrystalline LiBO_2 matrix. This selective modification of grain-boundary and pore structures provides a clear microstructural basis for understanding neutron-induced engineering of ion transport in LiBO_2 serving as an experimental model of PolySSICs in our current study, setting the stage for our discussion in subsequent sections.

To establish the relationship between crystal structure and microstructural evolution induced by thermal neutron irradiation, the diffraction results in Figure 2 are discussed in conjunction with the SEM and FIB–SEM observations in Figures 3 and 4. Powder x-ray diffraction (PXRD) patterns of the raw, pristine, and irradiated LiBO_2 samples show that the monoclinic LiBO_2 phase remains the dominant crystalline phase across all irradiation conditions examined, with no detectable formation of new crystalline phases within the resolution of the Rietveld refinement. Minor contributions from tetragonal $\text{Li}_2\text{B}_4\text{O}_7$ persist at a low level and remain essentially unchanged upon irradiation.

For the pristine pellet, the PXRD pattern (labeled in Fig. 2 as **pristine (PXRD)**) exhibits sharp diffraction peaks characteristic of long-range crystallographic order, consistent with the dense and well-connected polycrystalline microstructure observed in Figure 3. The corresponding GIXRD pattern of the pristine sample (labeled in Fig. 2 as **pristine (GIXRD)**) closely matches the bulk PXRD results, indicating that the near-surface re-

gion retains the same crystalline structure as the bulk. This structural uniformity is consistent with the SEM and FIB–SEM observations, which reveal intact grains, well-defined grain boundaries, and residual porosity.

After 10 minutes of thermal neutron irradiation, the PXRD patterns (labeled in Fig. 2 as **10 min (PXRD)**) continue to show well-defined diffraction peaks corresponding to monoclinic LiBO_2 , with no notable peak broadening or intensity loss that would indicate bulk amorphization or severe lattice disorder. This confirms that the long-range crystallographic framework of LiBO_2 remains largely intact at this irradiation dose. Similarly, the GIXRD pattern (labeled in Fig. 2 as **10 min (GIXRD)**) of the 10-minute irradiated sample shows no discernible changes compared to the pristine surface, suggesting that even though crater-like microstructures can be observed with SEM on the surface, the crystallographic order is largely unaffected or any changes are below the detection limit of our X-ray diffraction analyses.

Taken together, the combined PXRD, GIXRD, and microstructural analyses demonstrate that short-duration thermal neutron irradiation selectively modifies the near-surface and grain-boundary regions of polycrystalline LiBO_2 while preserving its long-range crystalline order. This decoupling between bulk structural integrity and localized microstructural evolution provides a critical foundation for understanding how thermal neutron irradiation affects the structure and microstructure of polycrystalline LiBO_2 , and hence its ion transport.

3.2 Effects of Irradiation Dose on Structure and Microstructure of LiBO_2

The evolution of the LiBO_2 system under increasing thermal neutron exposure reveals a clear correlation between irradiation dose and microstructural modification, even as the long-range crystallographic order remains remarkably resilient. As established in Fig. 2, the characteristic PXRD peaks for monoclinic LiBO_2 persist across all dosage levels—from the pristine state through 10, 60, 120, and up to 720 minutes of irradiation which are labeled in Fig. 2 as **pristine (PXRD)**, **10 min (PXRD)**, **60 min (PXRD)**, **120 min (PXRD)**, and **720 min (PXRD)**, respectively—indicating that the bulk crystal

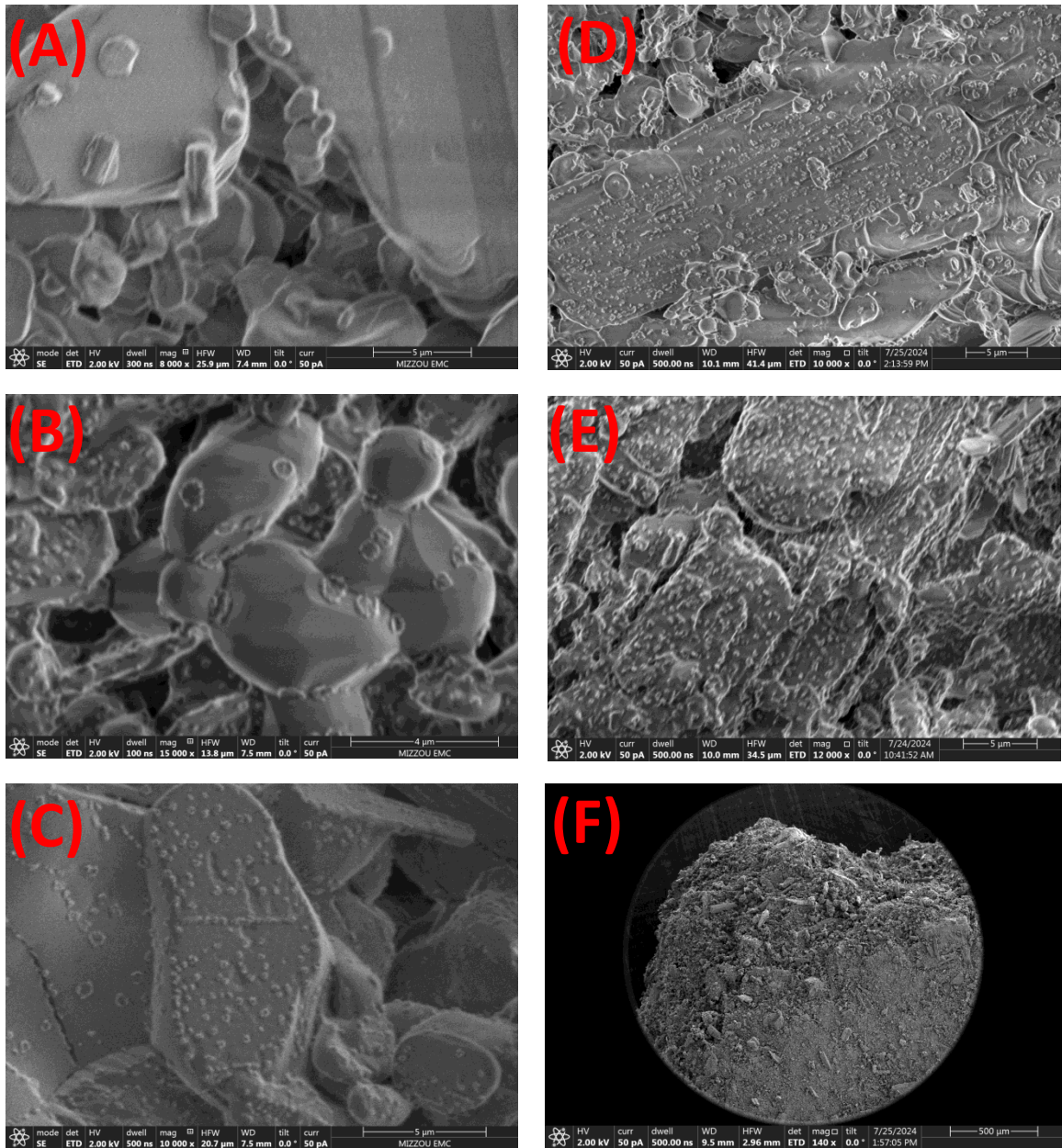


Figure 5: Dose-dependent Microstructure of LiBO_2 .

framework does not undergo complete amorphization. As a result, the Rietveld refinement for all of the diffraction patterns shows that the lattice parameters and weight fractions of the two crystal phases slightly fluctuate around their average values [major monoclinic LiBO_2 (94 ± 3 %): $a = 5.84 \pm 0.01$ Å, $b = 4.35 \pm 0.02$ Å and $c = 6.46 \pm 0.02$ Å, $\beta = \gamma = 90^\circ$ and $\alpha = 115.02 \pm 0.18^\circ$; and minor tetragonal $\text{Li}_2\text{B}_4\text{O}_7$ (6 ± 3 %): $a = b = 9.47 \pm 0.04$ Å and $c = 10.32 \pm 0.13$ Å]. In other words, no clear dose-dependent trend is found from the lattice parameters obtained from the refinement, suggesting that the monoclinic lattice remains largely intact, even under prolonged exposure to thermal neutrons.

However, a detailed examination of the microstructure in Figure 5 (panels A–E) highlights a progressive accumulation of surface and interface modifications, which is summarized as follows:

- **Pristine to Short-Term Exposure (0–10 min):** As shown in Figure 3 and panel A of Figure 5, the pristine sample starts as a dense polycrystalline network with well-defined grains and residual porosity. After 10 minutes (Figure 4 and panel B of Figure 5), the initial effects of neutron capture by ^{10}B and ^6Li manifest as localized crater-like features and enlarged pore mouths. These craters are non-uniformly distributed, preferentially forming at triple junctions and grain boundaries where the lattice is naturally more susceptible to displacement cascades. A more detailed discussion of the microstructural contrast between pristine and 10-min irradiated pellets can be seen in the previous section (Section 3.1).
- **Intermediate Exposure (60–120 min):** With increased irradiation time to 60 minutes (panel C of Figure 5) and 120 minutes (panel D of Figure 5), there is a noticeable increase in the density and size of these surface craters. Localized energy deposition from energetic particles (e.g., alpha particles, γ photons, and recoil ions) leads to more extensive material ejection and the interconnection of subsurface voids. This suggests that while the grains themselves remain structurally coherent, the "plumbing" of the material—its grain boundaries and outgassing pathways—is being significantly modified.
- **Extended Exposure (720 min/12 h):** At the highest dose of 720 minutes (panel E of Figure 5), the cumulative stress from helium buildup, lattice vacancies, and

thermal spikes reaches a critical threshold. While Figure 2 confirms that the LiBO_2 phase is still present, the physical integrity of the pellet is compromised. This is most evident in panel F of Figure 5, which shows the result of a 720-minute irradiation where the pellet suffered macroscopic fracture. The transition from localized surface cratering to bulk mechanical failure at 12 hours suggests that the prolonged generation of transmutation by-products eventually overcomes the cohesive strength of the polycrystalline framework.

In summary, the irradiation dose acts as a precision tool for defect engineering at lower exposures (up to 120 min) by selectively modifying ion transport channels at grain boundaries. However, excessive doses lead to a "saturation" of defects that results in the mechanical breakdown of the material, marking the upper dose limit that can be optimally set for effective neutron-induced engineering of ion transport in LiBO_2 without compromising the the integrity of whole solid pellets.

3.3 Effects of Irradiation Dose on Ionic Conductivity

As described in the Introduction (Section 1), the primary objective of this work is to demonstrate that thermal neutron irradiation can serve as a controllable defect-engineering strategy to selectively modify ion transport in LiBO_2 , leading to its enhanced ionic conductivity. Specifically, neutron-induced defects (e.g., Li and B vacancies) are expected to alter ionic migration pathways and thereby enhance the overall ionic conductivity (see also Fig. 1). This section presents and discusses the effects of irradiation time on ion transport in grains and grain boundaries of polycrystalline LiBO_2 pellets subjected to thermal neutron radiation.

To quantify these effects, electrochemical impedance spectroscopy (EIS) measurements were performed at room temperature on all pristine and irradiated pellets using symmetric blocking aluminum electrodes (upper inset, right panel of Fig. 6). The measurements were conducted over the frequency range from 1 mHz to 1 MHz, and the resulting Nyquist plots are shown in Fig. 6A. The experimental data (symbols) were fitted (solid lines) using an appropriate equivalent circuit model (lower inset, Fig. 6B), enabling extraction of the ionic conductivities associated with the grain interiors (σ_1) and the grain boundaries (σ_2).

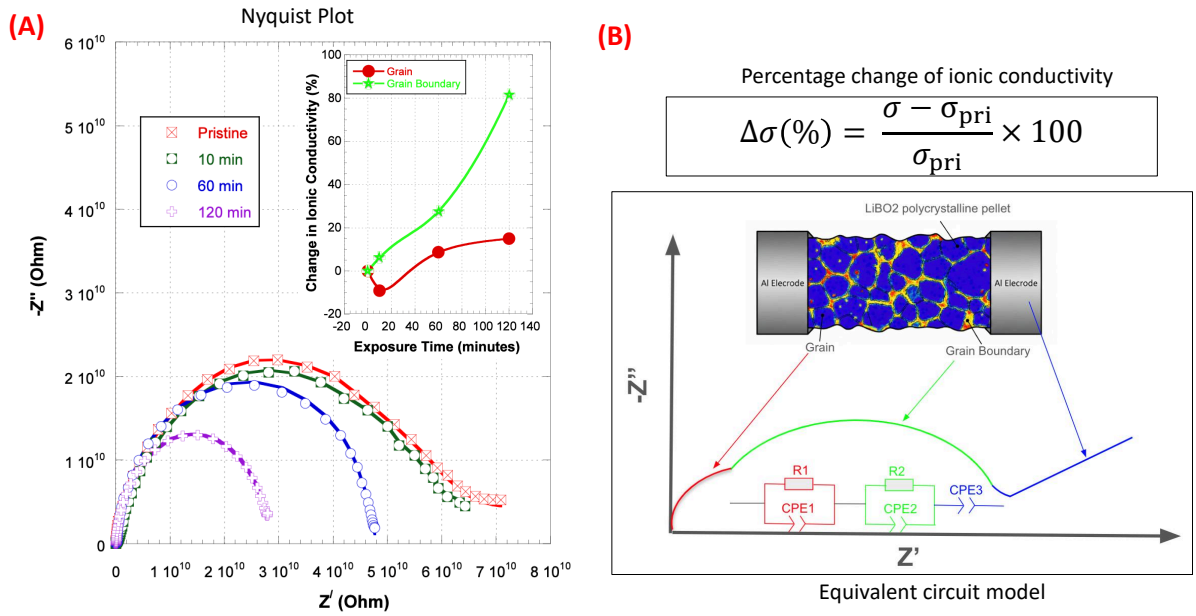


Figure 6: Dose-dependent EIS and ionic conductivity of LiBO_2 .

The impedance response of a polycrystalline LiBO_2 pellet [93]—consistent with typical polySSIC behavior [35–37, 94–98]—can be interpreted using an equivalent electrical circuit consisting of two resistor–constant phase element (R–CPE) units connected in series, followed by an additional CPE in series [35–37, 93–100]:

$$(R_1 \parallel CPE_1) - (R_2 \parallel CPE_2) - CPE_3. \quad (3)$$

Here, the subscript “1” corresponds to the high-frequency response of the grain (bulk) interior, while “2” represents the medium-frequency contribution of grain boundaries. The third element, CPE_3 , accounts for low-frequency electrode polarization effects (see schematic Nyquist plot in Fig. 6B).

The grain ionic conductivity is determined from the extracted grain resistance R_1 as

$$\sigma_1 = \frac{L}{R_1 A}, \quad (4)$$

where $L = 1.6$ cm and $A \approx 2$ cm² are the thickness of the pellet and its cross-sectional area, respectively.

It is noted that the constant phase element (CPE) was introduced to model non-ideal capacitive behavior commonly observed in polycrystalline materials. Its complex impedance is defined as

$$Z_{\text{CPE}} = \frac{1}{Q(j\omega)^n} = \frac{1}{Q\omega^n} \exp\left(-j\frac{n\pi}{2}\right), \quad (5)$$

hence, the complex impedance of a R -CPE in parallel is given by

$$Z_{R\parallel\text{CPE}}(\omega) = \frac{1}{\frac{1}{R} + Q(j\omega)^n}, \quad (6)$$

which can be separated into its real and imaginary components as

$$Z'(\omega) = \frac{R(1 + (RQ\omega^n) \cos(\frac{n\pi}{2}))}{1 + 2(RQ\omega^n) \cos(\frac{n\pi}{2}) + (RQ\omega^n)^2}, \quad (7)$$

$$Z''(\omega) = -\frac{R(RQ\omega^n) \sin(\frac{n\pi}{2})}{1 + 2(RQ\omega^n) \cos(\frac{n\pi}{2}) + (RQ\omega^n)^2}, \quad (8)$$

where j is the imaginary unit, ω is the angular frequency, Q is the CPE constant, and $0 < n \leq 1$ is a dimensionless exponent describing the deviation from ideal capacitive behavior (with $n = 1$ corresponding to an ideal capacitor).

The effective capacitance associated with a CPE–resistor pair can be estimated as

$$C = (R^{1-n}Q)^{1/n}, \quad (9)$$

from which the grain-boundary ionic conductivity can be determined as

$$\sigma_2 = \frac{L}{R_2 A} \frac{C_1}{C_2} = \frac{L}{R_2 A} \frac{(R_1^{1-n_1} Q_1)^{1/n_1}}{(R_2^{1-n_2} Q_2)^{1/n_2}}. \quad (10)$$

In addition, for irradiated samples, the corresponding conductivities are denoted as $\sigma_{1,\text{irr}}$ and $\sigma_{2,\text{irr}}$, while those of pristine samples are $\sigma_{1,\text{pri}}$ and $\sigma_{2,\text{pri}}$. The relative conductivity change was calculated as

$$\Delta\sigma_i(\%) = \frac{\sigma_{i,\text{irr}} - \sigma_{i,\text{pri}}}{\sigma_{i,\text{pri}}} \times 100, \quad i = 1, 2. \quad (11)$$

All fitting parameters obtained from the EIS analysis of the pristine and irradiated pellets are provided in Figure 7 in the Appendix. For the pristine pellet, the fitted grain resistance is $R_1 = 1.0 \times 10^7 \Omega$ (10 M Ω), which is approximately three orders of magnitude smaller than the grain-boundary resistance, $R_2 = 5.1 \times 10^{10} \Omega$ (51 G Ω). This large dif-

ference is attributed to the formation of a space-charge region at the grain boundaries arising from the accumulation of positively charged oxygen vacancies, as suggested by our Energy-Dispersive X-ray (EDS) spectroscopy data (see Figure 8 in the Appendix). Such grain-boundary blocking effects have been observed in some of PolySSICs. For example, Wu and Guo [95] reported an even stronger grain-boundary blocking effect (approximately four orders of magnitude) in the perovskite $\text{Li}_{3x}\text{La}_{2/3-x}\text{O}_{1/3-2x}\text{TiO}_{3-\delta}$ ($3x = 0.263$), where the large disparity between grain and grain-boundary ionic conductivities was attributed to positively charged space-charge layers at grain boundaries, which can be partially neutralized by dynamically introduced electrons. Experimental strategies to mitigate grain-boundary blocking in PolySSICs include increasing the annealing temperature during solid-state synthesis [96], deliberate grain-boundary engineering [97], grain-boundary amorphization [98], and irradiation with ionizing radiation (e.g., ultraviolet (UV) or gamma rays) [35–37].

In the present work, we demonstrate for the first time that thermal neutron transmutation can serve as an alternative strategy to mitigate grain-boundary blocking. During thermal neutron irradiation, the transmutation reactions of ${}^6\text{Li}$ and ${}^{10}\text{B}$ generate cascades and subcascades of atomic displacements, accompanied by the emission of energetic particles and gamma photons. These processes promote the redistribution of atoms and electrons, which likely leads to partial neutralization of the space charge in the grain-boundary region, thereby reducing the impedance to Li^+ ion transport across grain boundaries. In particular, electrons displaced or liberated by gamma photons produced as by-products of the ${}^{10}\text{B}$ transmutation may contribute to this neutralization mechanism (see Fig. 1). The reversible neutralization of grain-boundary space charge by electrons excited by gamma and UV photons has previously been reported by Deferriere et al. [35, 36]. In contrast, in the present study we observe that the structural, microstructural, and electrical modifications of LiBO_2 pellets occur in a nonreversible and dose-dependent manner. Specifically, compared with the pristine pellets ($R_2 = 51.0 \text{ G}\Omega$), pellets irradiated with thermal neutrons for 10, 60, and 120 minutes exhibit progressively reduced grain-boundary resistance values of 48.0, 40.0, and 28.1 $\text{G}\Omega$, corresponding to reductions of 5.9%, 21.6%, and 44.9%, respectively. It is noted that the pellets irradi-

ated for 720 minutes (12 h) fractured due to helium buildup resulting from transmutation reactions and therefore could not be characterized by EIS.

In contrast to the monotonic reduction observed for the grain-boundary resistance, the effect of irradiation dose on the grain (bulk) resistance exhibits a gradual and nonmonotonic behavior. Relative to the pristine pellet ($R_1 = 10\text{M}\Omega$), the grain resistance values for samples irradiated with thermal neutrons for 10, 60, and 120 minutes are 11, 9.2, and 8.7 $\text{M}\Omega$, corresponding to relative changes of +10%, -8%, and -13%, respectively (where the sign indicates an increase or decrease with respect to the pristine value).

The initial increase in R_1 after 10 minutes of irradiation suggests that, at low defect concentrations, irradiation-induced lattice defects such as Li and B vacancies remain spatially isolated and therefore act predominantly as scattering or trapping centers for mobile Li^+ ions, slightly impeding intra-grain ion transport. As the irradiation dose increases, however, the defect population becomes sufficiently dense for these vacancy sites to form a connected network that enables vacancy-mediated Li^+ diffusion across the grain interior. This transition from isolated defects to an interconnected defect landscape can facilitate long-range percolative Li^+ transport, thereby reducing the bulk resistance.

This interpretation is consistent with the conclusions drawn by Deck and Hu [60], who showed that entropy-driven disorder enhances Li^+ mobility primarily by weakening local Li^+ -anion interactions; however, a substantial increase in macroscopic ionic conductivity emerges only when such local disorder becomes integrated into thermodynamically stable, extended structures that support percolating diffusion pathways. The present experimental observation is also consistent with density functional theory predictions [23, 24], which indicate that high concentrations of boron vacancies in LiBO_2 can significantly reduce the migration energy barrier for Li^+ ions via a vacancy-mediated diffusion mechanism. Importantly, these lattice vacancies are energetically unfavorable under equilibrium synthesis conditions and therefore difficult to achieve through conventional defect-engineering approaches such as solid-state reactions. Thermal neutron irradiation thus provides a unique non-equilibrium pathway for generating such defects, enabling controlled modification of the ion transport landscape within the crystal lattice.

Finally, the percentage changes in the ionic conductivities obtained from Eqn. (11)

were then plotted as functions of the irradiation time to show the effects of the irradiation dose on the ionic conductivity (see the inset of Fig. 6A). It is clearly seen that the ionic conductivity is increased by nearly 20% for the grains and more than 80% for the grain boundaries.

4. Conclusions

In summary, we demonstrate experimentally for the first time that high-flux thermal neutrons delivered at Beam Port E of the University of Missouri Research Reactor (MURR), rather than within the reactor core, can selectively drive nuclear transmutation reactions in the strong neutron-absorbing isotopes ^{10}B and ^6Li , which are uniformly incorporated into the LiBO_2 crystal lattice at their natural isotopic abundances of $\sim 19.9\%$ and $\sim 7.5\%$, respectively. These neutron-capture processes (Fig. 1) generate lattice vacancies while largely preserving the long-range crystallographic framework of the host material. Concurrently, γ photons emitted as products of the ^{10}B transmutation reactions liberate bonded electrons that help mitigate irradiation-induced atomic displacement through electron-stopping processes. These liberated electrons can also partially compensate the space-charge regions associated with positively charged oxygen vacancies at grain boundaries, thereby modifying the ion transport landscape and resulting in increases in ionic conductivity of nearly 20% within the grains and more than 80% across the grain boundaries.

Beyond LiBO_2 , the approach presented here establishes a potential general framework for nuclear defect engineering in polycrystalline solid-state ionic conductors (PolySSICs), enabling access to defect configurations that are thermodynamically inaccessible through conventional synthesis routes. This strategy opens new opportunities for simultaneously tuning enthalpic and entropic contributions to ion transport and provides an important complement to existing chemical and structural engineering methodologies for advanced solid-state ionic devices such as those for energy conversion and storage technologies. Further systematic studies on LiBO_2 and a broader class of PolySSICs are warranted to explore thermal neutron irradiation—either as a standalone technique or in synergy with conventional synthesis approaches—to fully realize the potential of this emerging

| Sample | Grain | | | Grain Boundary | | | Electrode | |
|----------|-------------------------|-------|----------------------------|-------------------------|-------|----------------------------|------------------------|-------|
| | Q_1 (10^{-10}) | n_1 | R_1 ($10^6 \Omega$) | Q_2 (10^{-10}) | n_2 | R_2 ($10^9 \Omega$) | Q_3 (10^{-8}) | n_3 |
| pristine | 0.32 | 0.98 | 10 | 0.80 | 0.90 | 51.0 | 0.7 | 0.60 |
| 10 min | 0.55 | 0.98 | 11 | 0.75 | 0.90 | 48.0 | 0.7 | 0.60 |
| 60 min | 0.25 | 0.98 | 9.2 | 0.97 | 0.98 | 40.0 | 12 | 0.60 |
| 120 min | 0.82 | 0.98 | 8.7 | 0.95 | 0.95 | 28.1 | 3.1 | 0.60 |

Figure 7: Fitting Parameters of EIS data modeling for pristine and irradiated LiBO_2 .

defect-engineering strategy.

Appendix

This Appendix provides additional supporting data (see Fig. 7 and Fig. 8) for discussion in Section 3.3.

Data Availability

It is officially and firmly stated that the raw and reduced data that support the findings of this study are available from the corresponding authors upon reasonable request. The outputs and parameters obtain during Rietveld refinement of our XRD data and electric circuit model fitting of the reduced EIS data for the current study have been archived and can be shared with interested researchers to facilitate replication or further exploration of the results.

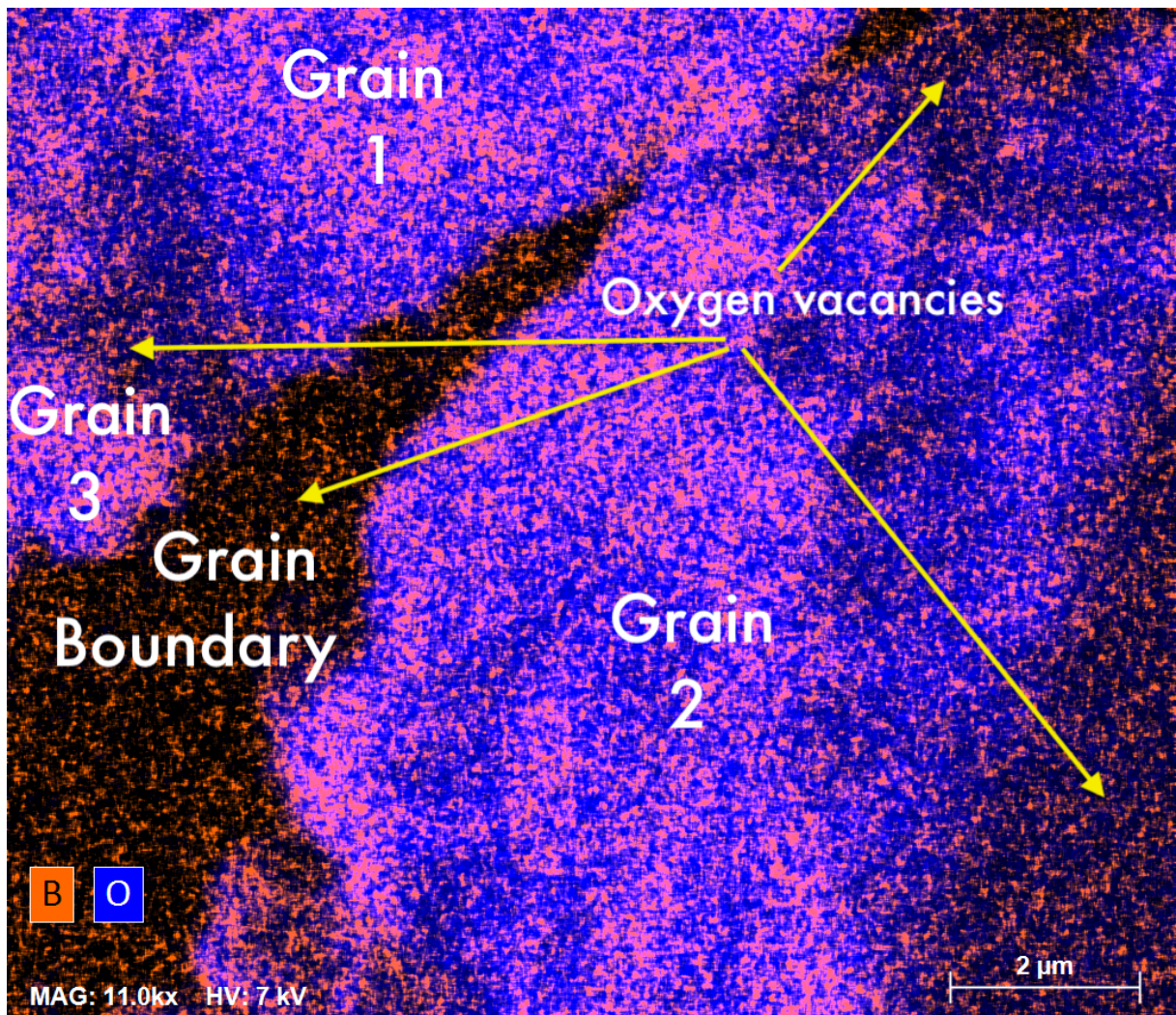


Figure 8: Energy-Dispersive X-ray Spectroscopy (EDS) of the surface of a pristine LiBO_2 pellet.

Author Information

Corresponding Authors

** These are corresponding authors, to whom all issues pertaining to this work should be addressed via their contact information listed here:

Ha M. Nguyen - Institute of Materials Science and Engineering, University of Missouri, Columbia, MO 65201, USA;

Email: hn4gq@missouri.edu; Phone: (+1) 573-882-5939.

Thomas W. Heitmann - University of Missouri Research Reactor (MURR), University of Missouri, Columbia, MO 65201, USA;

Email: heitmannt@missouri.edu; Phone: (+1) 573-884-9309.

Yangchuan Xing - Department of Chemical and Biomedical Engineering, University of Missouri, Columbia, MO 65201, USA;

Email: xingy@missouri.edu; Phone: (+1) 573-884-1067.

Authors

Carson D. Ziemke - Department of Physics and Astronomy, University of Missouri, Columbia, MO 65201, USA.

David Stalla - Electron Microscopy Core, University of Missouri, Columbia, MO 65201, USA.

Bikash Saha - University of Missouri Research Reactor (MURR), University of Missouri, Columbia, MO 65201, USA.

Narendrakumar Narayanan - University of Missouri Research Reactor (MURR), University of Missouri, Columbia, MO 65201, USA.

Sebastián Amaya-Roncancio - Grupo de Simulación de Materiales, Escuela de Física, Universidad Pedagógica y Tecnológica de Colombia, Avenida Central del Norte 39-115, Boyacá, 150003, Tunja, Colombia.

Carlos Wexler - Department of Physics and Astronomy, University of Missouri, Columbia, MO 65201, USA.

John Gahl - University of Missouri Research Reactor (MURR), University of Missouri, Columbia, MO 65201, USA.

Author Contributions

* H.M.N and C.D.Z are the authors who contributed equally to the work. Principal Investigators (C.W, J.G., Y.X, T.W.H.); Conceptualization (C.W, J.G., Y.X, T.W.H., H.M.N); Sample preparation, x-ray diffraction and Rietveld (H.M.N, C.D.Z., N.N., T.W.H); SEM and FIB-SEM (C.D.Z., D.S, H.M.N); EIS (H.M.N., C.D.Z., Z.R.V, B.S.), Thermal-neutron Irradiation (C.D.Z., J.G., T.W.H., H.M.N.); Data presentation and manuscript writing (H.M.N.); manuscript reviewing and editing (all authors).

Notes

The authors declare no conflict of interest. All authors discussed, reviewed, edited, agreed, and were informed of the publication of the manuscript.

Acknowledgements

This work was funded by the University of Missouri Materials Science and Engineering Institute (MUMSEI) Grant No. CD002339, and the University of Missouri Research Reactor (MURR).

References

- [1] O. Yamamoto, *Solid state ionics: a Japan perspective*, Sci. Technol. Adv. Mater. **18** (2017) 504.
- [2] K. Funke, *Solid State Ionics: from Michael Faraday to green energy—the European dimension*, Sci. Technol. Adv. Mater. **13** (2013) 043502.

- [3] H. Rickert, *Solid Ionic Conductors : Principles and Applications*, Angew. Chem. Int. Ed. Engl. **17** (1978) 37.
- [4] Kazuya Terabe *et al.*, *Solid state ionics for the development of artificial intelligence components*, Japanese Journal of Applied Physics **61** (2022) SM0803
- [5] Erica Truong *et al.*, *Accelerating ion transport in polycrystalline conductors: On pores and grain boundaries*, Sci. Adv. **11** (2025) eadt7795.
- [6] A. K. Mishra *et al.*, *Review—inorganic solid state electrolytes: insights on current and future scope*, J. Electrochem. Soc. **168** (2021) 080536.
- [7] I. Riess, *Mixed ionic–electronic conductors—material properties and applications*, Solid State Ionics **157** (2003) 1.
- [8] J. Sunarso *et al.*, *Mixed ionic–electronic conducting (MIEC) ceramic-based membranes for oxygen separation* Journal of Membrane Science **320** (2008) 13.
- [9] A. Kızılbaşlan *et al.*, *Mixed ion-electron conductive materials: A path to higher energy density all-solid-state lithium-ion batteries*, Nano Today **60** (2025) 102556.
- [10] Shuvajit Ghosh *et al.*, *A Review on High-Capacity and High-Voltage Cathodes for Next-Generation Lithium-ion Batteries*, Journal of Energy and Power Technology **4** (2022) 1-59.
- [11] Wen-hui Hou *et al.* Recent Advances in Electrolytes for High-Voltage Cathodes of Lithium-Ion Batteries, Transactions of Tianjin University **29** (2023) 120–135.
- [12] B. Xu *et al.*, *Recent progress in cathode materials research for advanced lithium ion batteries*, Mater. Sci. Eng.: R: Reports **7** (2012) 51.
- [13] C. M. Hayner *et al.*, *Materials for Rechargeable Lithium-Ion Batteries*, Annu. Rev. Chem. Biomol. Eng. **3** (2012) 445.
- [14] Alex K. Koech *et al.*, *Lithium-ion battery fundamentals and exploration of cathode materials: A review*, South African Journal of Chemical Engineering **50** (2024) 321.

- [15] B. Yuanyuan et al., *Research progress on cathode materials for lithium-ion batteries*, Journal of Solid State Electrochemistry **29** (2025) 3595.
- [16] Peiyuan Guan et al., *Recent progress of surface coating on cathode materials for high-performance lithium-ion batteries*, Journal of Energy Chemistry **43** (2020) 220-235.
- [17] U. Nisar et al., *Valuation of Surface Coatings in High-Energy Density Lithium-ion Battery Cathode Materials*, Energy Storage Materials **38** (2021) 309.
- [18] Xinru Tan et al., *Recent progress in coatings and methods of Ni-rich $\text{LiNi}_{0.8}\text{Co}_{0.1}\text{Mn}_{0.1}\text{O}_2$ cathode materials: A short review*, Ceramics International **46** (2020) 21888–21901.
- [19] Gurbinder Kaur et al., *Review-Surface Coatings for Cathodes in Lithium Ion Batteries: From Crystal Structures to Electrochemical Performance*, Journal of the Electrochemical Society **169** (2022) 043504.
- [20] Varad A. Maske and Aarti P. More, *Conformal coatings for lithium-ion batteries: A comprehensive review* Progress in Organic Coatings **188** (2024) 108252.
- [21] Z. Chen et al., *Role of surface coating on cathode materials for lithium-ion batteries*, J. Mater. Chem. **20** (2010) 7606.
- [22] Shenzhen Xu, Ryan M. Jacobs, Ha M. Nguyen, Shiqiang Hao, Mahesh Mahanthappa, Chris Wolvertond, and Dane Morgan, *Lithium transport through lithium-ion battery cathode coatings*, J. Mater. Chem. A (2015) 17248–17272.
- [23] Carson D. Ziemke, Ha M. Nguyen, Sebastian Amaya-Roncancio, John Gahl, Yangchuan Xing, Thomas W. Heitmann, and Carlos Wexler, *Formation of lattice vacancies and their effects on lithium-ion transport in LiBO_2 crystals: comparative ab initio studies*, J. Mater. Chem. A **13** (2025) 3146–3162.
- [24] Ha M. Nguyen, Carson D. Ziemke, Narendrakumar Narayanan, Sebastian Amaya-Roncanci, John Gahl, Yangchuan Xing, Thomas W. Heitmann, Carlos Wexler,

- Vacancy-induced Modification of Electronic Band Structure of LiBO₂ Material as Cathode Surface Coating of Lithium-ion Batteries*, Mater. Adv. **6** (2025) 6682-6693.
- [25] M. Guo *et al.*, *Excellent electrochemical properties of Ni-rich LiNi_{0.88}Co_{0.09}Al_{0.03}O₂ cathode materials co-modified with Mg-doping and LiBO₂-coating for lithium ion batteries*, New Journal of Chemistry **47** (2023) 968-2977.
- [26] D. Wang *et al.*, *Multifunctional Li₂O-2B₂O₃ coating for enhancing high voltage electrochemical performances and thermal stability of layered structured LiNi_{0.5}Co_{0.2}Mn_{0.3}O₂ cathode materials for lithium ion batteries*, Electrochim. Acta **174** (2015) 1225-1233.
- [27] M. Du *et al.*, *Enhanced high-voltage cycling stability of Ni-rich LiNi_{0.8}Co_{0.1}Mn_{0.1}O₂ cathode coated with Li₂O-2B₂O₃*, J. Alloys Compd. **805** (2019) 991-998.
- [28] S. Gao *et al.*, *Boron Doping and LiBO₂ Coating Synergistically Enhance the High-Rate Performance of LiNi_{0.6}Co_{0.1}Mn_{0.3}O₂ Cathode Materials*, CS Sustainable Chem. Eng. **9** (2021) 5322-5333.
- [29] Xin-Kang Li *et al.*, *Synergistic LiBO₂/CeF₃ hybrid coating engineering for chemically stabilized cathode-electrolyte interphase in nickel-rich cathodes*, Rare Met. **44** (2025) 7254-7266.
- [30] X. Zhang *et al.*, *An effective LiBO₂ coating to ameliorate the cathode/electrolyte interfacial issues of in LiNi_{0.6}Co_{0.2}Mn_{0.2}O₂ solid-state Li batteries*, Journal of Power Sources **426** (2019) 242-249.
- [31] B. Ramkumar *et al.*, *LiBO₂-modified LiCoO₂ as an efficient cathode with garnet framework Li_{6.75}La₃Zr_{1.75}Nb_{0.25}O₁₂ electrolyte toward building all-solid-state lithium battery for high-temperature operation*, Electrochimica Acta **359** (2020) 136955.
- [32] Tianming Li and Kai Xiao *Solid-State Iontronic Devices: Mechanisms and Applications*, Advanced Materials Technologies **7** (2022) 2200205.

- [33] F.H. Garzon *et al.*, *Solid state ionic devices for combustion gas sensing*. Solid State Ionics **175** (2004) 487-490.
- [34] M. Kleitz *et al.*, *Solid state ionics for advanced chemical sensors*, Solid State Ionics **Volume 18–19, Part 1**(1986) 98.
- [35] Thomas Defferriere *et al.*, *Photo-enhanced ionic conductivity across grain boundaries in polycrystalline ceramics*, Nature Materials **21** (2022) 438–444.
- [36] Thomas Defferriere *et al.*, *Ionic conduction-based polycrystalline oxide gamma ray detection-radiation-ionic effects*, Adv. Mater. **36** (2024) 200.
- [37] Thomas Defferriere and Harry L Tuller, *Optoionics: New opportunity for ionic conduction-based radiation detection*, MRS Commun. **15** (2025) 523–532.
- [38] Kazuya Terabe *et al.* *Solid state ionics for the development of artificial intelligence components*, Jpn. J. Appl. Phys. **61** (2022) SM0803
- [39] Yangyin Chen, *ReRAM: History, Status, and Future*, IEEE Transactions on Electron Devices **67** (2020) 420 - 1433.
- [40] Suhas Kumar *et al.*, *Dynamical memristors for higher-complexity neuromorphic computing*, Nature Reviews Materials **7** (2022) 575–591.
- [41] Xiaojun Zeng *et al.*, *Progress and challenges of ceramics for supercapacitors*, Journal of Materiomics **7** (2021) 1198-1224.
- [42] Javed Rehman *et al.*, *A Review of Proton-Conducting Electrolytes for Efficient Low-Temperature Solid Oxide Fuel Cells: Progress, Challenges, and Perspectives*, Energy & Fuels **38** (2024) 22637–22665.
- [43] Muhammad Faizan *et al.*, *Ion transport mechanism in sodium-ion batteries: Fundamentals, applications, and future trends*, Journal of Energy Storage **122** (2025) 116616.
- [44] Huggins A. Robert, *Advanced batteries-materials science aspects* (Springer, 2009).

- [45] Gary S. Was, *Fundamentals of Radiation Material Science: Metals and Alloys* (Springer-Verlag Berlin Heidelberg, 2007).
- [46] Helmut Mehrer, *Diffusion in Solids: Fundamentals, Methods, Materials, Diffusion-Controlled Processes* (Springer-Verlag Berlin Heidelberg, 2007).
- [47] J. P. Riviere, *Radiation Induced Point Defects and Diffusion in Application of Particle and Laser Beams in Materials Technology* edited by P. Misaelides (Springer, 1995).
- [48] W. Hayes (Author) and A. M. Stoneham (Author), *Defects and Defect Processes in Nonmetallic Solids* (book), (Dover Publications, 2004).
- [49] D. P. Almond and A. R. West, *The activation entropy from transport in ionic conductors*, *Solid State Ionics* **23** (1987) 27-35.
- [50] Yong-jun Zhang, *Entropy and ionic conductivity*, *Physica A* **391** (2012) 4470-4475.
- [51] Yuan Ren *et al.*, *Relationship between ion transport and entropy in the solid electrolyte Li_3ErCl_6 based on the thermodynamics and density functional theory calculation*, *Journal of Energy Storage* **141** (2026) 119372.
- [52] Yanlong Wu *et al.*, *Exploiting the mixed entropy strategy for the design of fast ion conductors*, *Adv. Energy Mater.* **14** (2024) 2401528
- [53] J. Mi *et al.*, *Defect Strategy in Solid-State Lithium Batteries*, *Small Methods* **8** (2024) 1.
- [54] Xuyong Feng *Review of modification strategies in emerging inorganic solid-state electrolytes for lithium, sodium, and potassium batteries*, *Joule* **6** (2022) 543–587.
- [55] Huangxu Li *et al.*, *The concept of high entropy for rechargeable batteries*, *Progress in Materials Science* **148** (2025) 101382.
- [56] Shengyang Dong *et al.*, *High-entropy oxides: Emergent materials for electrochemical energy storage and conversion*, *Journal of Materials Science & Technology* **227** (2025) 192-215.

- [57] Jincan Li *et al.*, *High-entropy materials: Excellent energy-storage and conversion materials in the field of electrochemistry*, *Particuology* **92** (2024) 42-60.
- [58] Y. Zeng *et al.*, *High-Entropy Mechanism to Boost Ionic Conductivity*, *Science* **378** (2022) 1320-1324.
- [59] Chuan Wang *et al.*, *Accelerating lithium ion transport via increasing the entropy of the electrolyte for stable lithium metal batteries*, *Journal of Energy Chemistry* **99** (2024) 384-392.
- [60] Michael J. Deck and Yan-Yan Hu *Leveraging local structural disorder for enhanced ion transport*, *Journal of Materials Research* **38** (2023) 2631-2644.
- [61] Zhizhen Zhang and Linda F. Nazar *Exploiting the paddle-wheel mechanism for the design of fast ion conductors*, *Nature Reviews Materials* **7** (2022) 389–405.
- [62] Harender S. Dhatarwal, Rahul Somni and Richard C. Remsing, *Electronic paddle-wheels in a solid-state electrolyte*, *Nature Communications* **15** (2024) 121.
- [63] Bowen Chen *et al.*, *Li-stuffed garnet electrolytes: structure, ionic conductivity, chemical stability, interface, and applications*, *Can. J. Chem.* **100** (2022) 311–319.
- [64] Xiong Wang *et al.*, *Understanding the key role of cocktail effect in high-entropy materials for Li-ion and Na-ion batteries*, *Energy Storage Materials* **84** (2026) 104819.
- [65] Zhipeng Wang *et al.*, *Cocktail Effects in Boosting the Interfacial Ionic Conduction of the Garnet Solid-State Battery*, *ACS Appl. Mater Interfaces* **17** (2025) 28103-28114.
- [66] Shuo Wang *et al.*, *Frustration in Super-Ionic Conductors Unraveled by the Density of Atomistic States*, *Angew. Chem. Int. Ed.* **62** (2023) e202215544.
- [67] Brandon C. Wood *et al.*, *Paradigms of frustration in superionic solid electrolytes*, *Philos. Trans. A. Math. Phys. Eng. Sci.* **379** (2021) 20190467.
- [68] Roman Schlem *et al.*, *Energy Storage Materials for Solid-State Batteries: Design by Mechanochemistry*, *Adv. Energy Mater.* **11** (2021) 2101022.

- [69] G. H. Kinchin and R. S. Pease, *The Displacement of Atoms in Solids by Radiation*, Rep. Prog. Phys. **18** (1955) 1.
- [70] Tristan Olsen *et al.*, *Radiation effects on materials for electrochemical energy storage systems*, Phys. Chem. Chem. Phys. **25** (2023) 30761.
- [71] M. Kuhnke *et al.*, *Defect Generation in Crystalline Silicon Irradiated with High Energy Particles*, Internet link: <https://rd48.web.cern.ch/technical-notes/rosetn01-05.pdf>
- [72] M. M. Rahman *et al.*, *Defect and structural evolution under high-energy ion irradiation informs battery materials design for extreme environments*, Nature Communications **11** (2020) 4548.
- [73] C. Tan *et al.*, *Radiation effects on the electrode and electrolyte of a lithium-ion battery*, Journal of Power Sources **318** (2016) 242-250.
- [74] L. Li *et al.*, *Neutron radiation on tin anodes of lithium-ion batteries*, Radiation Effects and Defects in Solids: Incorporating Plasma Science and Plasma Technology **173** (2018) 1068-1074.
- [75] Mazharul M. Islam *et al.*, *The ionic conductivity in lithium-boron oxide materials and its relation to structural, electronic and defect properties: insights from theory*, J. Phys.: Condens. Matter **24** (2012) 203201.
- [76] Igor N. Ogorofnikov *et al.*, *Radiation effects and defects in lithium borate crystals*, IOP Conf. Series: Materials Science and Engineering **15** (2010) 012016.
- [77] M. Haseman *et al.*, *Neutron irradiation induced defects in oxides and their impact on the oxide properties*, Journal of Applied Physics **129** (2021) 215901.
- [78] Jie Qiu *et al.*, *Effects of neutron and gamma radiation on lithium-ion batteries*, Nuclear Instruments and Methods in Physics Research B **345** (2015) 27-37.
- [79] I. S. Shlimak, *Neutron transmutation doping in semiconductors: science and applications*, Phys. Solid State **41** (1999) 716.

- [80] J. V. Logan *et al.*, *Potential for neutron and proton transmutation doping of GaN and Ga₂O₃*, Mater. Adv. **1** (2020) 45.
- [81] R. Barber, Q. Nguyen, J. Brockman, J. Gahl, and J. Kwon, *Thermal neutron transmutation doping of GaN semiconductors*, Scientific Reports **10** (2020) 16295.
- [82] M. Tanenbaum and A. D. Mills, *Preparation of uniform resistivity n-type silicon by nuclear transmutation*, J. Electrochem. Soc. **108** (1961) 171–176.
- [83] A. Y. Polyakov *et al.*, *Neutron transmutation doping effects in GaN*, J. Vac. Sci. Technol. B **28** (2010) 608.
- [84] K. Kuriyama *et al.*, *Lattice distortions and the transmuted-Ge related luminescence in neutron-transmutation-doped GaN*, Phys. Lett. **80** (2002) 3328.
- [85] I. Lee *et al.* *Deep electron and hole traps in neutron transmutation doped n-GaN*, J. Vac. Sci. Technol. B **29** (2011) 041201.
- [86] M. Satoh *et al.*, *Depth uniformity of electrical properties and doping limitation in neutron-transmutation-doped semi-insulating GaAs*, J. Appl. Phys. **67** (1990) 3542.
- [87] Elena Echeverria *et al.*, *Lithium Tetraborate as a Neutron Scintillation Detector: A Review*, Crystals textbf14 (2024) 61.
- [88] R.M. Walker, *On the production of displaced atoms by thermal neutrons*, Journal of Nuclear Materials **2** (1960) 147-151.
- [89] John D. Brockmanan *et al.*, *A new single-crystal filtered thermal neutron source for neutron capture therapy research at the University of Missouri*, International Conference on Reactor Physics, Nuclear Power: A Sustainable Resource, Casino-Kursaal Conference Center, Interlaken, Switzerland, September 14-19, 2008, link: <https://inldigitallibrary.inl.gov/sites/sti/sti/4074899.pdf>
- [90] John D. Brockmanan *et al.*, *Computational characterization and experimental validation of the thermal neutron source for neutron capture therapy research at the*

University of Missouri, International Conference on Mathematics and Computational Methods Applied to Nuclear Science & Engineering, (M&C 2013), Sun Valley, Idaho, USA, May 5-9, 2013. Link <https://www.osti.gov/biblio/22212753>

- [91] John D. Brockmanan *et al.*, *Characterization of a boron neutron capture therapy beam line at the University of Missouri Research Reactor*, J. Radioanal. Nucl. Chem. **282** (2009) 157–160.
- [92] J. Minkiewicz *et al.*, *Large-scale manufacturing of solid-state electrolytes: Challenges, progress, and prospects*, Open Ceramics **16** (2023) 100497.
- [93] Eiichi Hirose *et al.*, *Lithium ionic conductivities of α -LBO₂ with two-dimensional Li-Li networks and γ -LBO₂ with three-dimensional ones synthesized under high pressure*, Journal of Solid State Chemistry **274** (2019) 100-104.
- [94] S. R. Hui *et al.*, *A Brief Review of the Ionic Conductivity Enhancement for Selected Oxide Electrolytes*, J. Power Sources **172** (2007) 493.
- [95] Jian-Fang Wua and Xin Guo, *Origin of the low grain boundary conductivity in lithium ion conducting perovskites: $Li_{3x}La_{0.67-x}TiO_3$* , Phys. Chem. Chem. Phys. **19** (2017) 5880.
- [96] C. W. Ban and G. M. Choi, *The effect of sintering on the grain boundary conductivity of lithium lanthanum titanates*, Solid State Ionics **140** (2001) 285–292.
- [97] Tomasz Polczyk *et al.*, *Mitigation of grain boundary resistance in $La_{2/3-x}Li_{3x}TiO_3$ perovskite as an electrolyte for solid-state Li-ion batteries*, J. Mater. Sci. **56** (2021) 2435–2450.
- [98] Yanlin Zhu *et al.*, *Reduced Energy Barrier for Li^+ Transport Across Grain Boundaries with Amorphous Domains in LLZO Thin Films*, Nanoscale Research Letters **15** (2020) 153.
- [99] Alexandros Ch. Lazanas and Mamas I. Prodromidis, *Electrochemical Impedance Spectroscopy-A Tutorial*, ACS Meas. Sci. Au **3** (2023) 162-193.

- [100] Pooja Vadhva *Electrochemical Impedance Spectroscopy for All-Solid-State Batteries: Theory, Methods and Future Outlook*, ChemElectroChem **8** (2021) 1930-1947.